

# RSC Advances



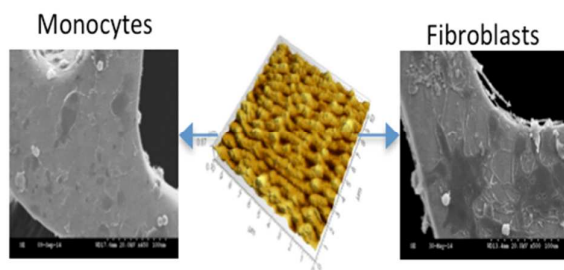
This is an *Accepted Manuscript*, which has been through the Royal Society of Chemistry peer review process and has been accepted for publication.

*Accepted Manuscripts* are published online shortly after acceptance, before technical editing, formatting and proof reading. Using this free service, authors can make their results available to the community, in citable form, before we publish the edited article. This *Accepted Manuscript* will be replaced by the edited, formatted and paginated article as soon as this is available.

You can find more information about *Accepted Manuscripts* in the [Information for Authors](#).

Please note that technical editing may introduce minor changes to the text and/or graphics, which may alter content. The journal's standard [Terms & Conditions](#) and the [Ethical guidelines](#) still apply. In no event shall the Royal Society of Chemistry be held responsible for any errors or omissions in this *Accepted Manuscript* or any consequences arising from the use of any information it contains.

Cell attachment and growth can be controlled by stent surface topography. In some cases fibroblast cells attach while monocytes failed on the structured surface of Pt:SS and 316LSS stents.



## In-Vitro Study on the Response of RAW264.7 and MS-5 Fibroblast cells on Laser-Induced Periodic Surface Structures for Stainless Steel Alloys

Clare McDaniel<sup>1</sup>, Olga Gladkovskaya<sup>1,2</sup>, Aiden Flanagan<sup>3</sup>, Yury Rochev<sup>2</sup> and Gerard M. O'Connor<sup>1</sup>

<sup>1</sup>NCLA/Inspire Laboratories, School of Physics, National University of Ireland Galway, University Road, Galway, Ireland

<sup>2</sup>National University of Ireland, Galway, Network of Excellence for Functional Biomaterials (NFB), School of Chemistry, Galway, Ireland

<sup>3</sup>Boston Scientific – Galway Ballybrit Business Park Ballybrit, Galway, Ireland

**Keywords:** LIPSS, Laser Induced Periodic Surface Structures, metal, alloy, platinum, 316L Stainless Steel, femtosecond laser, RAW 264.7, MS-5 Fibroblast, cells.

### **Abstract**

The manner in which cells interact with a surface is mainly determined by the surface chemistry, surface charge, curvature and micro-topography of the surface. This study investigates the bio response of two metallic alloy coronary stents with Laser Induced Periodic Surface Structures (LIPSS) produced by femtosecond laser pulses at 515 nm and 1030 nm wavelengths. The study relates the bio response to changes in micro-topography and chemical composition.

LIPSS were generated in this study by applying femtosecond pulses with a 500 fs pulse duration at a high repetition rate to smooth polished Platinum Stainless Steel (Pt:SS) and 316LSS stent surfaces, with an original roughness value of  $2.9 \pm 0.2$  nm and  $1.5 \pm 0.2$  nm respectively. LIPSS structures were formed by exposure to laser radiation slightly above the applied threshold fluence using a Gaussian laser beam in air. Experiments were performed at two different wavelengths, 1030 nm and 515 nm, to generate different periodic topographies. When the laser wavelength is increased the LIPSS period and depth also increases, thereby increasing the roughness. LIPSS features were characterized using techniques such as Atomic Force Microscopy (AFM) and X-ray Photoelectron Spectroscopy (XPS).

This study identifies how LIPSS impact the attachment of monocyte cells (RAW 264.7) and fibroblast cells (MS-5) in vitro. The cellular reactions of un-textured to LIPSS surfaces were compared. It was found using Scanning Electron Microscopy (SEM) that different cells either attached or detached to LIPSS roughness (ranging from 29 nm to 50 nm). Fibroblast cells did not adhere to un-textured surfaces but formed a monolayer on LIPSS surfaces. This indicates that the LIPSS surface is non-toxic. Monocytes show a high affinity to bare un-textured surfaces and failed to firmly attach onto textured surfaces. In the case of stents, it is an advantage that the concentration of monocytes decreases when LIPSS are introduced as this can reduce thrombosis occurring. In the future, laser structured surfaces with various topographies can offer new bio-functionalities in the area of medical implants.

## 1. Introduction

Cardiovascular disease is a generic name for the family of disorders related to blood vessels. They can lead to heart problems such as heart attack or stroke. Atherosclerosis causes narrowing or blockage of the blood vessel which results in deterioration of cardio-system functions. Implanting a stent can treat the stenosed artery. A stent is a small wire mesh tube that acts as a scaffold used to mechanically hold open the blood vessel. In recent years, drug-eluting stents (DES) have been developed to decrease restenosis. LIPSS could be beneficial to DES. Incorporating a complex surface topography could encourage endothelialisation and limit thrombotic events.

Lasers have been chosen in this study to generate LIPSS and using these structures the cell response can be evaluated. A number of processes can be performed with lasers: cutting, welding, drilling ablation, melting and marking. Lasers offer excellent precision and repeatability, high speed and quality, accuracy, cost efficiency, minimal thermal input and non-contact. Laser processing has gained significant credibility in the medical device industry and is an integral part of manufacturing, for example, cutting surgical tools, welding endoscopes or pacemaker housings, drilling holes in hypodermic needles and verification laser marking. Of particular relevance to this study is the application of lasers to profile stents. Femtosecond lasers are ideal for surface structuring because they have a minimal heat affected zone, there is rapid heating and cooling and no laser plasma interaction. Laser Induced Periodic Surface Structures, otherwise known as “ripples”, have been fabricated on metal,<sup>1-4</sup> polymer,<sup>5</sup> semiconductor,<sup>6</sup> and dielectric<sup>7</sup> surfaces and have been significantly studied since the 1960s. The formation of LIPSS depends on several factors, such as: wavelength, laser fluence, repetition rate, the number of pulses and the angle of the incident laser beam. With metals, LIPSS normally have a period close to the wavelength of the incident beam and are orientated perpendicular to the direction of the polarization of the beam. It has been recently found that materials such as semiconductors, dielectrics and metals achieve LIPSS with a period much smaller than the laser wavelength.<sup>8</sup> The spatial period of the LIPSS is dependent on the angle of incidence, wavelength and polarization of the laser beam.<sup>9</sup> LIPSS have a number of applications like increasing the surface area and surface energy, altering the hydrophilic or hydrophobic performance of a materials surface,<sup>10</sup> improving coating adhesion, optics, reducing reflectivity,<sup>11</sup> and tribology.<sup>12, 13</sup> The chemical composition and topography of a surface has the greatest effect on protein adsorption.<sup>14</sup> By increasing the surface area there is expected to be an increase in protein adsorption. The mechanisms responsible for ripple formation are still under debate today. There are a number of theories that attempt to explain the formation of LIPSS. Examples of these include excitation of surface plasmon polaritons (SPPs),<sup>8</sup> self-organization,<sup>15</sup> the interference between the laser beam and the scattered wave from the surface material<sup>1</sup> and the influence of surface tension.<sup>16, 17</sup> Advantages of using LIPSS in this study is that the surface area of a material can be increased in air quickly without the aid of

chemicals and stents can be fabricated with various topographies depending on the desired application.

*In-vitro* bio systems were used to model the response of immune cells that circulate in the blood stream of a blood vessel. RAW264.7 cells represent peripheral blood circulating monocytes. Their primary function is monitoring and first line defense against foreign bodies. MS-5 fibroblasts originate from connective tissue and are used in this study to model the response of a blood vessel exposed to a stent.

Monocyte and fibroblast cell types are used in this study to investigate the biocompatibility of a biomaterial, in this case clinically approved stent material. Monocyte adhesion and infiltration occurs instantaneously after injury to the artery. RAW264.7 is a monocyte cell line which fully possesses immune responses including activation into macrophages, expression pro-inflammatory surface markers, inflammatory proteins and stimuli for T-cell recruitment. RAW264.7 murine monocyte/macrophage cells have been used in a number of *in-vitro* biomaterial studies.<sup>18, 19</sup> RAW264.7 offer diversity in a number of applications: monocytes can be converted to osteoclasts in the presence of receptors for nuclear factor kappa B ligand (RANKL).<sup>20</sup> In addition they are easy to transfect and activate into mature macrophage phenotype. Alternatively, RAW264.7 cells can be used as naive monocytes. They have been used to describe biomaterial properties, such as capacity to trigger inflammatory response<sup>21</sup> or suppress macrophages,<sup>22</sup> attract circulating monocytes, ingestion by immune cells, facilitate cell adhesion and growth as immune cells or osteoclasts. It has been found that RAW264.7 cells display a higher rate of adhesion on smooth surfaces compared to rougher surface where the cells begin to differentiate.<sup>23</sup> Other studies that investigated the performance of RAW264.7 cells on smooth and rough surfaces did not give a definitive answer: some groups suggested that monocytes have an affinity to smooth surfaces,<sup>24, 25</sup> while others reported no difference,<sup>26</sup> or others observed monocyte activation on flat samples.<sup>27</sup> Lee et al<sup>27</sup> found a higher concentration of monocyte cells present on the surface of textured titanium, with a roughness value of 4.76 nm, compared to un-textured samples, with a roughness value of 0.37 nm.

Fibroblast cells are connective tissue cells that play a crucial role in wound healing. MS-5 murine fibroblast cells do not have direct applications in *in-vitro* studies, but they have positive effects on vasculogenesis and haemopoiesis.<sup>28</sup> Fibroblast cells are one of the most common cells used in *in vitro* biomaterial testing and have been used to investigate stent surfaces in previous studies.<sup>29, 30</sup> Also they promote growth of primitive haematopoietic progenitor CD34+ human cord blood cells<sup>31</sup> and differentiation of murine embryonic stem cells.<sup>32</sup> It has been found that fibroblast cells adhered more to smooth samples compared to laser treated 316LSS samples.<sup>33</sup> On Silicone, it was found that fibroblast growth decreases with increasing surface roughness (smooth 88 nm, rough from 378 nm to 650 nm).<sup>34</sup> Pennisi et al<sup>35</sup> found

that fibroblast cells are more elongated and their cytoskeleton is less mature on rough platinum surfaces (11 nm) compared to smooth surfaces (0.65 nm). The growth rate decreases as the surface roughness increases (11nm to 23 nm). Li et al<sup>36</sup> found that after laser texturing of 316LSS there was a reduction in cytotoxicity for endothelial cells grown on laser-textured surfaces compared to un-textured surfaces. They also found using XPS that the surface chemistry changes with 316LSS LIPSS. There was a reduction in the concentration of iron and nickel with an increase in chromium. To our knowledge the cellular interaction with LIPSS structures of different topographies on metal alloys has not been investigated to date.

## 2. **Materials & Methods**

### 2.1 Materials

This study focuses on two alloys; 316L Stainless Steel (SS) and Pt:SS. Pt:SS is composed of 316L stainless steel with the addition of platinum. The overall composition of Pt:SS comprises of 33% Platinum, 37% Iron, 18% Chromium, 9% Nickel, 3% Molybdenum and traces of Manganese. Platinum is used because it creates stronger and more flexible stent struts. Platinum based Stainless Steel alloys are useful due to their resistance to corrosion and high melting temperatures. 316LSS is a Chromium-Nickel-Molybdenum alloy consisting of 61-72% Iron, 16-18% Chromium, 10-14% Nickel, 2-3% Molybdenum, 2% Manganese, 0.08% Carbon, 0.75% Silicon, 0.45% Phosphorus, 0.03% Sulphur and 0.1% Nitrogen. 316L stainless steel is known for its strength, biocompatibility and it is relatively easy to machine due to the carbon present. Metallic stents are preferred because of their radiopacity properties. The Pt:SS and 316LSS stents used in this study have been electro-polished to create smooth  $R_a$  surfaces with an average roughness value of  $2.9 \pm 0.2$  nm and  $1.5 \pm 0.2$  nm respectively. The curvature of the Pt:SS and 316LSS struts are calculated as  $9.02 \pm 0.64$  mm<sup>-1</sup> and  $8.59 \pm 0.22$  mm<sup>-1</sup>, respectively. The characteristics of a stent are different to a flat sample. Studies performed on stent materials, in vivo, have limitations due to the stent size, pattern and curvature and the challenge to analyse the contact angle, surface energy and cell behaviour.

### 2.2 Laser Processing

Pt:SS and 316LSS surfaces were exposed to multiple incident laser shots in air at a repetition rate of 100 kHz at various pulse energies ranging from 2  $\mu$ J to 6  $\mu$ J. Experiments were carried out using a Yb:KYW chirped-pulse-regenerative amplification laser system (Amplitude Systemes S-pulse HP) that delivered laser pulses with a duration of approximately 500 fs at wavelengths of 1030 nm and 515 nm. The spatial profile of the laser was Gaussian in nature with a nominal  $M^2$  value of <1.2. The number of pulses is controlled using a computer controlled fast electro-optical modulator (EOM). The pulse energy was controlled using a rotary half-wave plate and a beam splitting polarizing cube.

The process of fully textured stents with LIPSS is shown in figure 1. The stent is placed on a 0.051" mandrel. This mandrel is held at one side by a rotary stage and the other side by a collet. A rectangular array consisting of 45,000 laser spots was fabricated on the stent slightly above the threshold fluence. Each spot was exposed to 30 successive laser pulses. The stent was then rotated using a motion system. This procedure was repeated until the stent was fully textured with LIPSS.



**Figure 1** Stent on mandrel held together by two collets (one in a rotary stage) on an XYZ stage.

The calculations for determining applied threshold fluence ( $\phi_{th}$ ) and  $\omega_0$  are obtained according to the method of Liu et al.<sup>37</sup> The spatial fluence,  $\phi(r)$ , for a Gaussian beam is given by:

$$\phi(r) = \phi_0 e^{-2r^2/\omega_0^2} \quad (1)$$

where  $\phi_0$  is the peak fluence in the beam,  $r$  is the distance from the center of the beam and  $\omega_0$  is the Gaussian spot radius ( $1/e^2$ ). The maximum fluence and the pulse energy,  $E_p$ , are related by:

$$\phi_0 = \frac{2E_p}{\pi\omega_0^2} \quad (2)$$

The peak fluence is related to the diameter of the ablated spot:

$$D^2 = 2\omega_0^2 \ln\left(\frac{\phi_0}{\phi_{th}}\right) \quad (3)$$

where  $D^2$  is the maximum diameter of the damaged region zone. It is possible to determine the beam radius using the value for  $\omega_0$  from the plot of  $D^2$  versus the logarithm of the pulse energy. Once  $\omega_0$  is calculated fluence values can then be found using equation 3. By plotting  $D^2$  versus the natural log of the applied laser fluence and extrapolating the  $D^2$  line to zero,  $\phi_{th}$  can be calculated.<sup>37</sup> The representative diameters of the ablated spots were measured using an optical microscope three times to determine an average value.

### 2.3 Characterisation

LIPSS are generated slightly above the applied damage threshold fluence and then analysed using a SEM (Hitachi S2600N). The topography of the LIPSS were analysed using an AFM (Agilent 5500). The scan was performed using a contact mode tip (Nanosensors TM PPP-CONTR-10, resonance frequency 6-21 kHz, tip height 10-15  $\mu\text{m}$ , force constant 0.02-0.77 N/m). A 10  $\mu\text{m}^2$  area was performed at a

speed of 0.5 lines/s and a resolution of 1024. The surface roughness was calculated using PicoImage Advanced (Agilent Technologies) software. Chemical analysis was performed using XPS (Kratos Axis 165) to see if there is a change in the elemental composition with increasing laser pulses. Samples were exposed to 15 seconds of Ar cluster sputtering to decrease the carbon content present on the surface. The area of analysis was 110  $\mu\text{m}$  and selected at random. The XPS values are highly dependent on the location where the scan was obtained inside the spot.

#### 2.4 *Cell Adhesion Experiments*

The key challenge in design was to ensure the mandrels did not move during cell seeding and adhesion. Cells were seeded and incubated on stents placed on mandrels and clipped in place with stainless steel clips (Supacip 40, Rapesco) shown in figure 2. The mandrels were positioned on Teflon (1.5 mm thick), which was laser cut to allow no contact of Teflon to the stent, shown in figure 2. A Picosecond laser (Trumpf Trumicro 5050) was used at a repetition rate of 400 kHz at 1030 nm using 150 passes at 2.5 m/s. The laser was also used to create grooves on the Teflon to position and fix the mandrels in place. The Teflon holder allowed the stent to be as close to the bottom of the petri dish as possible. The clips kept the stent fixed in place to ensure no movement of the stent whereby cells could detach. A sufficient volume of cell culture media was used to ensure the stents were fully covered.

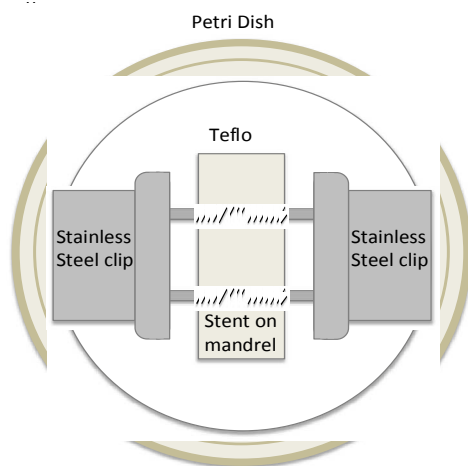


**Fig 2** *In vitro* stent holder.

RAW264.7 monocyte-macrophage and MS-5 fibroblast murine cell lines were used in this study. It is important to note that human pulmonary microvascular endothelial cells (HPMEC) were also investigated and showed a positive response to flat surfaces but as there was no difference between bare and rippled stents these results are not included in the current study. The images are available in the supplementary information, figure A. Cells were grown in Dulbecco's Modified Eagle Media (DMEM; Sigma), supplemented with 10% Foetal Bovine Serum (FBS; Sigma), 100  $\mu\text{g}/\text{mL}$  of penicillin and 100  $\mu\text{g}/\text{mL}$  of streptomycin. Cells were maintained in humidified atmosphere with 5%  $\text{CO}_2$  at 37  $^\circ\text{C}$ . On the day of the experiment,

confluent cell flasks were removed from the incubator. Cells were harvested using enzyme for fibroblasts or fluid wash for monocytes according to routine procedure. Cells were spun down at 1500 rpm for 5 minutes and the final cell pellet was re-suspended in fresh culture media. Cells were seeded onto the stent and left to attach for 6 hours in the incubator. Afterwards, the reduced media was removed and fresh aliquot was added. The next day, the samples were fixed with 2.5% glutaraldehyde and 2.5% paraformaldehyde in phosphate buffered saline (PBS) overnight at room temperature. The cells were then dehydrated in ascending dilutions of ethanol and critically point dried (Quorum Technologies K850 CPD). Samples were gold coated using a sputter coater (EMSCOPE SC500) and viewed under the SEM.

### 2.5 *Live/Dead Assay*

Cell viability was tested using a Live/Dead Assay (Live Technologies, Bio-Sciences, Dun Laoghaire, Ireland) according to the manufacturer protocol. Titration was performed for both calcein and ethidium bromide to define optimal dye concentration. RAW264.7 cells were seeded onto flat SS, Pt:SS stent and 316LSS stent samples in high ( $1 \times 10^6$  cells per well) concentrations. After 24 hours of co-culture, cell viability was examined. A Varioskan Flash plate reader was used to harvest a fluorescent signal from flat samples.

## 3. **Experimental Results**

### 3.1. *LIPSS*

Each stent was fully textured by combining an aligned array of spots at a laser wavelength of 515 nm and 1030 nm. Each spot was exposed to 30 successive laser pulses. The spot radius and threshold fluence were calculated using equations (2) and (3). The applied threshold fluence of Pt:SS for 1 pulse was previously calculated and it was found that with increasing number of laser pulses, the threshold fluence decreases.<sup>11</sup> The estimated applied threshold fluence of Pt:SS for 30 pulses at 1030 nm and 515 nm, are  $\phi_{th} = 0.12 \pm 0.02 \text{ J cm}^{-2}$  and  $0.10 \pm 0.01 \text{ J cm}^{-2}$  respectively. The applied threshold fluence of 316LSS for 30 pulses at 1030 nm and 515 nm, are  $\phi_{th} = 0.11 \pm 0.02 \text{ J cm}^{-2}$  and  $0.06 \pm 0.01 \text{ J cm}^{-2}$  respectively. There is a decrease in threshold fluence with decreasing laser wavelength. Pt:SS and 316LSS LIPSS were generated slightly above the applied threshold fluence at  $\phi = 0.2 \text{ J cm}^{-2}$  with 30 pulses for 515 nm and 1030 nm.

### 3.2. *AFM*

The topography of Pt:SS and 316LSS LIPSS on stents were analysed using AFM. Un-textured surfaces were compared against 515 nm and 1030 nm laser wavelength LIPSS. Changing the laser wavelength from IR to visible led to different LIPSS features such as various period and depth sizes thereby changing the roughness. The 3D and side profiles of each parameter are shown in figure 3. The grain structure of 316LSS is clearly visible in figure 3(d) with grains approximately 10-15  $\mu\text{m}$  in size. From table 1, there is an increase in the LIPSS period and depth with increasing

wavelength. In the case of Pt:SS the period has doubled, with an increase in depth of 105 nm, from 515 nm to 1030 nm. For 316LSS, the period has doubled, with an increase in depth of 64 nm, from 515 nm to 1030 nm. The largest estimated increase in surface area is 32% associated with Pt:SS 1030 nm LIPSS. There is an increase in the roughness with increasing wavelength. From 515 nm to 1030 nm, the surface roughness of Pt:SS has increased from  $35 \pm 3$  nm to  $50 \pm 3$  nm and of 316LSS has increased from  $29 \pm 2$  nm to  $48 \pm 3$  nm.

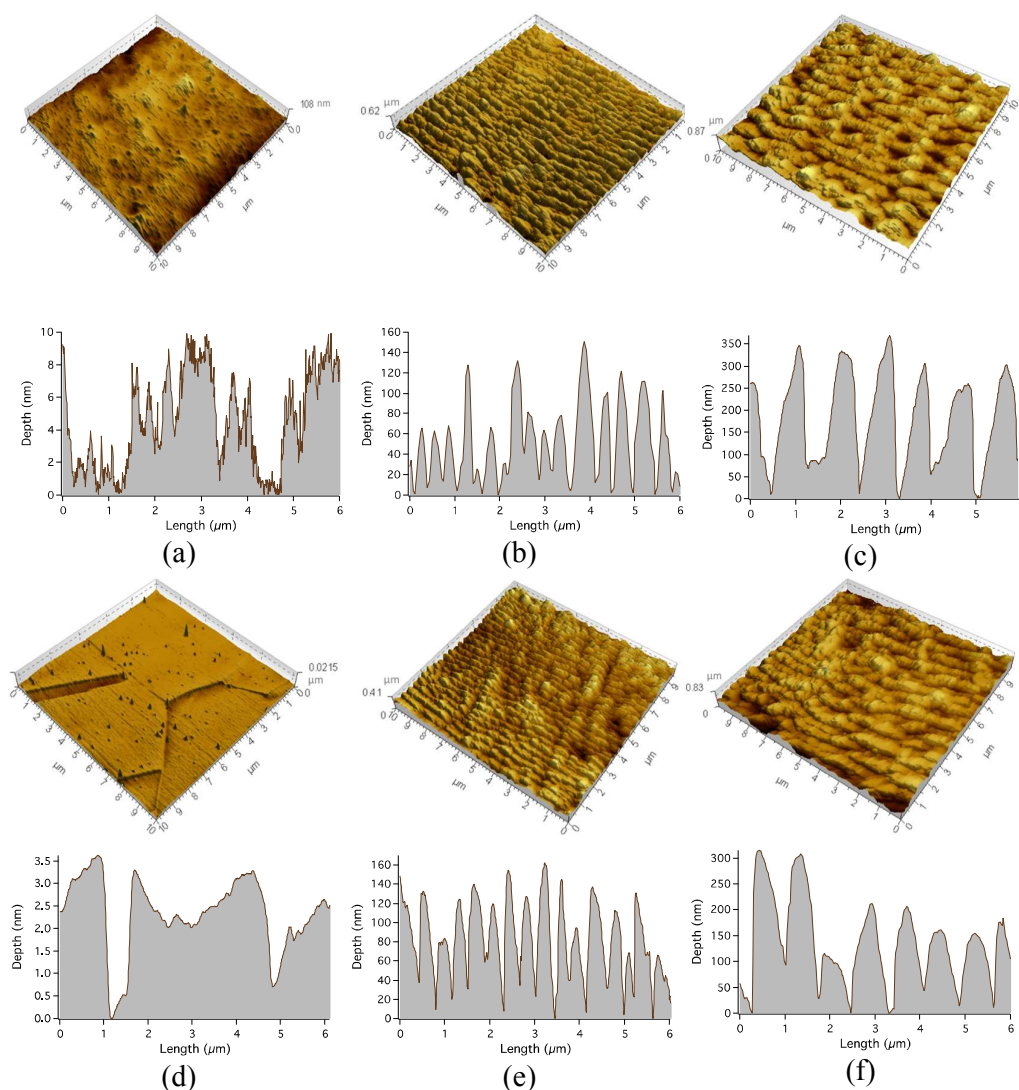


**Fig 3.** AFM topography of Pt:SS (a) un-textured, (b) 515 nm LIPSS and (c) 1030 nm LIPSS; 316LSS (d) un-textured, (e) 515 nm LIPSS and (f) 1030 nm LIPSS. LIPSS were generated at 100 kHz for 30 pulses at  $0.2 \text{ Jcm}^{-2}$ .

**Table 1.** LIPSS period, depth and roughness (using AFM) and surface area for Pt:SS and 316LSS after exposure to 30 pulses at a repetition rate of 100 kHz at  $0.2 \text{ Jcm}^{-2}$ .

	Pt:SS	316LSS
	<b>Un-textured</b>	
<b>Roughness, Ra (nm)</b>	$2.9 \pm 0.2$	$1.5 \pm 0.2$

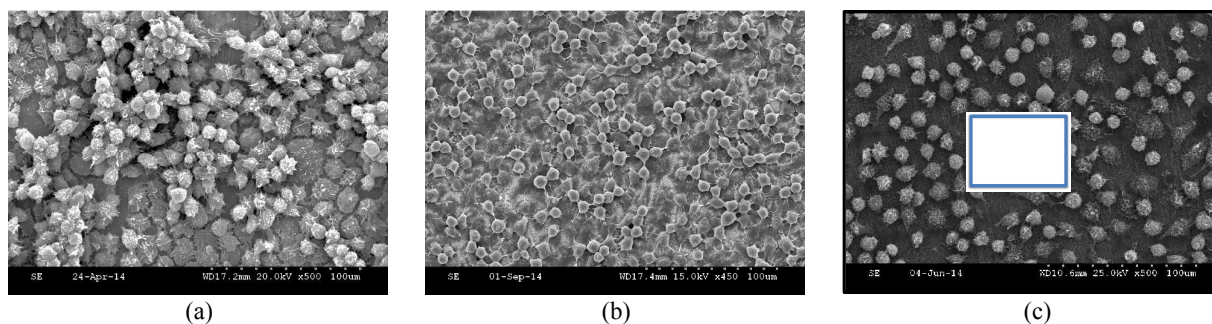
	515 nm	1030 nm	515 nm	1030 nm
<b>Roughness, Ra (nm)</b>	34.5 ± 3.3	49.6 ± 3.0	28.8 ± 1.6	47.9 ± 2.8
<b>Surface Area Increase(%)</b>	19.2 ± 0.9	32.5 ± 2.0	18.6 ± 1.7	25.9 ± 4.9
<b>Period (nm)</b>	388.7 ± 9.0	740.0 ± 13.9	360.0 ± 6.5	727.7 ± 16.9
<b>Depth (nm)</b>	86.1 ± 1.7	177.0 ± 5.2	77.8 ± 2.6	142.2 ± 4.7

### 3.3. *Live/Dead Assay*

A live/dead assay was performed on un-textured flat SS surfaces, 515 nm LIPSS and 1030 nm LIPSS of RAW 264.7 cells. LIPSS were generated using  $0.2 \text{ Jcm}^{-2}$  at 100 kHz. There is a high concentration on an un-textured flat surface, shown in figure 4(a). This verifies that the surfaces are non-cytotoxic. There is a decrease in the number of live cells attached to the surface with increasing LIPSS period and depth, shown in figures 4(b) and (c). Figure 4(d) is a magnified image of cells grown on 1030 nm LIPSS illustrating healthy morphologies. This implies that cells respond to a change in surface morphology or chemistry.

There is a decrease in the fluorescence of live cells (Calcein) with increasing LIPSS period and depth for 515 nm and 1030 nm, respectively, shown in figure 4(a-c). This is verified in the corresponding live/dead assay fluorescent values. The number of dead cells (Etdh) is insignificant in all cases. There is a high fluorescent value for bare media indicating that protein and fluorescent dye absorption has occurred on the metal; this suggests that it is not an effective control.

There are limitations with performing a live/dead assay on a stent surface due to the decreased surface area and the low concentration of adhered cells onto the surface. When this assay was performed on stents no signal was detected because the fluorescence was below the detection limit of the apparatus.



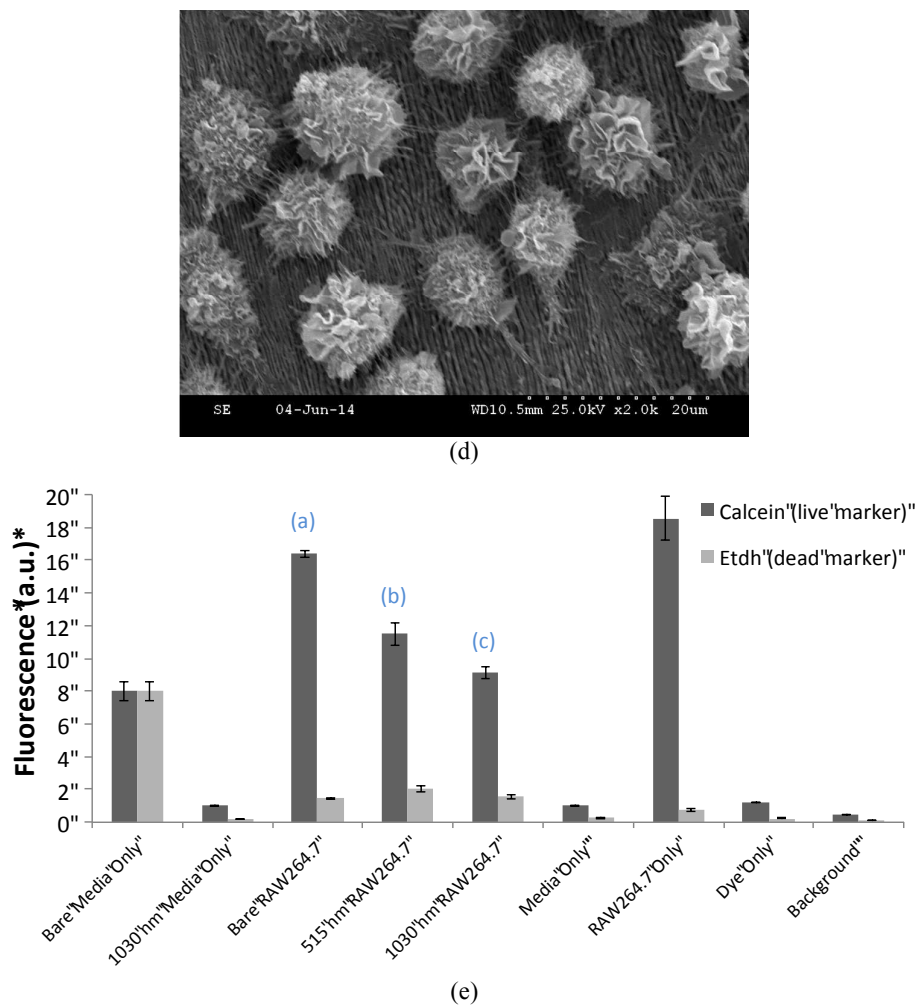


**Fig 4.** SEM images of RAW 264.7 on flat 316LSS (a) un-textured, (b) 515 nm LIPSS (c) 1030 nm LIPSS and (d) Zoomed area of 1030 nm LIPSS, shown as blue box in (c). The corresponding live/dead assay (e) performed using (a), (b) and (c).

### 3.4. SEM

SEM was used to visualize cell adhesion on the surface of the curved struts. Flat SS samples were used as a control to identify the role of curvature and eliminate surface area issues. Curved and flat samples that were treated with cell culture media only were used as a negative control. There appears to be minimal protein deposition on the curved control samples, shown in figures 5 and 6 for Pt:SS and 316LSS respectively.

As shown in figures 5 and 6, when a curved non-textured sample is introduced RAW264.7 monocytes attach onto the surface and grow without activating into macrophages. Following laser exposure, fibronectin threads can be easily seen between the cells, shown in figures iv(c). Also, large RAW264.7 clusters were found. In the case of fibroblasts, they failed to make a firm connection with the curved surface. With LIPSS covered stents, monocytes appear as single cells, loosely adhered to the surface in figures iii(b) and iii(c), with some cells undergoing

apoptosis. Fibroblasts formed a monolayer with healthy morphologies in the case of 1030 nm LIPSS unlike 515 nm LIPSS.

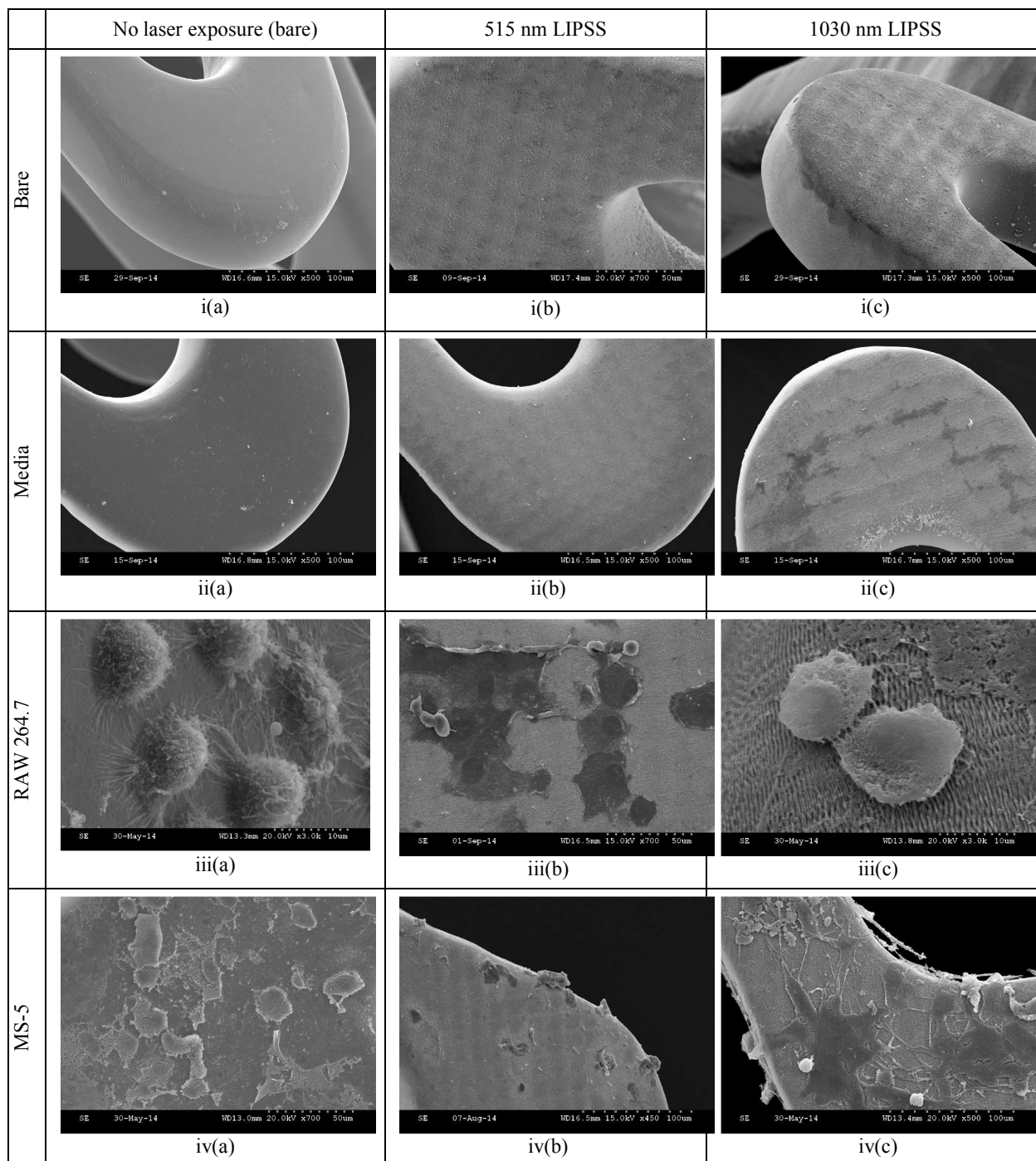


**Fig 5.** SEM images of Pt:SS stent un-textured i(a) bare, ii(a) media only, iii(a) RAW 264.7, iv(a) MS-5; Pt:SS 515 nm LIPSS i(b) bare, ii(b) media only, iii(b) RAW 264.7, iv(b) MS-5; Pt:SS 1030 nm LIPSS i(c) bare, ii(c) media only, iii(c) RAW 264.7 and iv(c) MS-5.

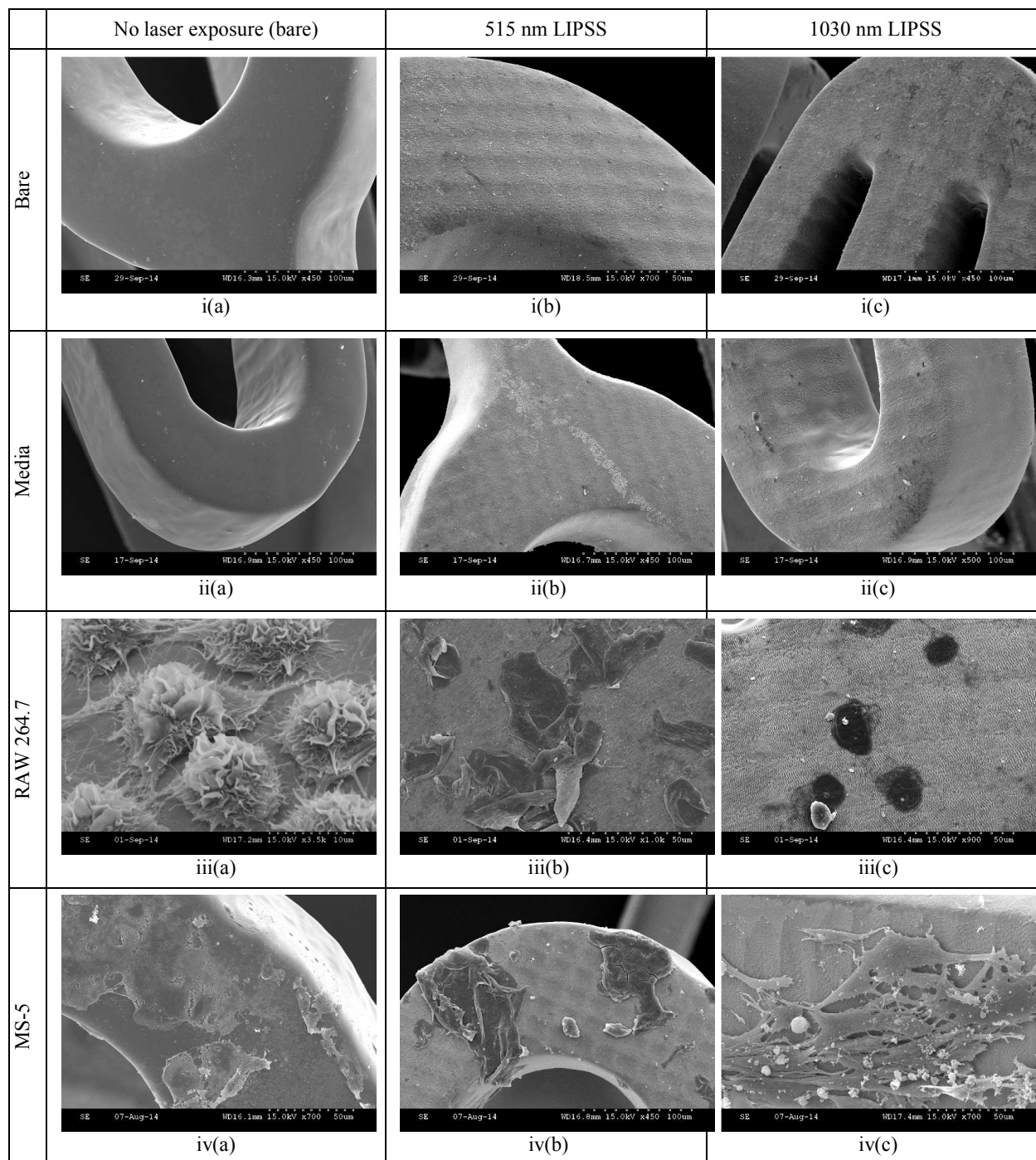


**Fig 6.** SEM images of 316LSS stent un-textured i(a) bare, ii(a) media only, iii(a) RAW 264.7, iv(a) MS-5; 316LSS 515 nm LIPSS i(b) bare, ii(b) media only, iii(b) RAW 264.7, iv(b) MS-5; 316LSS 1030 nm LIPSS i(c) bare, ii(c) media only, iii(c) RAW 264.7 and iv(c) MS-5.

### 3.5. Surface Chemistry

XPS was used to characterize the change in the elemental concentration of Pt:SS and 316LSS after femtosecond laser exposure. Table 2 illustrates the significant differences in concentrations between a bare un-textured surface, 515 nm LIPSS and 1030 nm LIPSS. The elements in Pt:SS 515 nm LIPSS that have the largest

percentage variation compared to un-textured Pt:SS are oxygen, iron and molybdenum. At 1030 nm, the leading percentage variations are oxygen, platinum and iron. The oxide layer has increased by 4.7% with 1030 nm LIPSS. For 316LSS, oxygen, nickel and molybdenum have the largest percentage variations at 515 nm. There is a difference response in iron and nickel between the two alloys. For 1030 nm, iron, chromium and molybdenum have the largest percentage difference. After femtosecond exposure, the surface chemistry for both alloys has changed.

**Table 2.** % Concentration for Pt:SS and 316LSS elements using XPS after exposure to 30 pulses at a repetition rate of 100 kHz at  $0.2 \text{ Jcm}^{-2}$ .

	Pt:SS (% Concentration)				
	No laser exposure (bare)	515 nm LIPSS	% Variation	1030 nm LIPSS	% Variation
O	$58.24 \pm 1.00$	$62.60 \pm 0.69$	+4.36	$62.91 \pm 0.87$	+4.67
Pt	$16.17 \pm 0.27$	$17.41 \pm 0.16$	+1.24	$11.12 \pm 0.18$	-5.05
Cr	$13.44 \pm 0.63$	$13.60 \pm 0.49$	+0.16	$12.95 \pm 0.51$	-0.49
Ni	$1.67 \pm 0.64$	$0.97 \pm 0.43$	-0.7	$0.14 \pm 0.61$	-1.53
Fe	$8.28 \pm 0.63$	$5.43 \pm 0.45$	-2.85	$9.89 \pm 0.65$	+1.61
Mo	$2.20 \pm 0.73$	$0.00 \pm 0.71$	-2.20	$2.99 \pm 0.81$	+0.79

	316LSS (% Concentration)				
	No laser exposure (bare)	515 nm LIPSS	% Variation	1030 nm LIPSS	% Variation
O	$70.56 \pm 1.00$	$74.59 \pm 1.03$	+4.03	$70.29 \pm 0.90$	-0.27
Cr	$16.79 \pm 0.61$	$16.52 \pm 0.46$	-0.27	$14.80 \pm 0.51$	-1.99
Ni	$1.86 \pm 0.84$	$0.24 \pm 0.58$	-1.62	$1.73 \pm 0.74$	-0.13
Fe	$8.27 \pm 0.69$	$8.07 \pm 0.62$	-0.2	$11.27 \pm 0.79$	+3.00
Mo	$2.52 \pm 0.49$	$0.59 \pm 0.42$	-1.93	$1.90 \pm 0.43$	-0.62

### **Discussion**

There is no measured difference in the applied threshold fluence for Pt:SS and 316LSS for 1030 nm based on 30 pulses, yet there is a decrease in  $\phi_{th}$  of  $0.10 \pm 0.01 \text{ J cm}^{-2}$  for Pt:SS and  $0.06 \pm 0.01 \text{ J cm}^{-2}$  for 316LSS for 515 nm. A decrease in threshold fluence with decreasing wavelength is found, which implies that there is less energy needed to ablate 316LSS at shorter wavelengths. This reduction can be attributed to changes in elemental composition or reflectivity.

AFM was used to analyse the LIPSS structures formed on Pt:SS and 316LSS. The period of the surface ripples is significantly smaller than the wavelength of the incident laser beam. In the case of Pt:SS, the period is estimated to be  $740 \pm 14 \text{ nm}$  and  $389 \pm 9 \text{ nm}$  when exposed to a 1030 nm and 515 nm laser beam, respectively. It was found that the LIPSS period increases with increasing laser wavelength. For a metal, the period of LIPSS ( $\Lambda$ ) is related to the wavelength using the equation<sup>38</sup>:

$$\Lambda = \frac{\lambda}{1 \pm \sin \theta} \quad (4)$$

where  $\lambda$  is the wavelength of the incident beam,  $\pm$  represents the back and forth propagating surface wave at the surface of the metal and  $\theta$  is the incident angle of the

laser on the surface of the material. Using equation 4,  $\Lambda$  is predicted accurately at  $\theta=25^\circ$  for 316LSS but does not capture the behaviour of Pt:SS.

The depth of the LIPSS also increases with increasing wavelength. The depth of ablation depends on the absorption coefficient, thermal diffusion and radiative cooling of the material. Because  $\alpha$  is very high for metals ( $\approx 10^6 \text{ cm}^{-1}$ ) the incident laser energy is absorbed between a 10-20 nm depth.<sup>39</sup> The effective penetration depth ( $\alpha^{-1}$ ) is proportional to the laser wavelength. For platinum,  $\alpha^{-1}$  is estimated to be 11 nm for 515 nm and 13 nm for 1030 nm. Hence, there is a marginal difference in depths between the incident wavelengths used in this study. Using AFM, for Pt:SS, the depth of LIPSS increased from  $86 \pm 2$  nm to  $177 \pm 5$  nm from a wavelength of 515 nm compared to 1030 nm; for 316LSS the depth has increased from  $78 \pm 3$  nm to  $142 \pm 5$  nm. This increase in depth found experimentally could be due to changes in the material after the laser interaction has ended. After exposure from a femtosecond pulse the alloy material is likely to become amorphous thereby changing its optical penetration depth.<sup>40-42</sup> Likewise, after multiple-pulse exposure incorporating rapid heating and cooling cycles, the alloy could evolve towards a metallic-like glass thus transforming the optical properties of the material.<sup>38</sup> This would allow for deeper surface structures.

The heat diffusion length,  $l_T$ , is calculated by  $2(D\tau_l)^{1/2}$  where  $D$  is the heat diffusivity and  $\tau_l$  is the laser pulse duration.<sup>38</sup> For stainless steel  $D$  is  $0.04 \text{ cm}^2/\text{s}$ <sup>38</sup> and within a laser pulse duration of 500 fs,  $l_T$  is calculated to be approximately 2 nm. For platinum ( $D = 0.25 \text{ cm}^2/\text{s}$ ),  $l_T$  is calculated to be 7 nm. The heat diffusion length within a laser pulse is underestimated and does not capture the depths measured using AFM. With multiple-pulse exposure, there could be an accumulation of heat, which increases in depth after each successive pulse thereby increasing the total depth of the LIPSS. Another factor that could contribute to a larger heat depth is the diffusion of ballistic electrons into the bulk of the material. Ballistic electrons are high-energy electrons that travel into the bulk of the material before thermalization.

The largest measured increase in surface area of 32% is associated with Pt:SS 1030 nm LIPSS and is attributed to the larger depth. Another measure of area, the surface roughness, has increased by approximately  $29.5 \pm 2.2$  nm and  $46.6 \pm 0.2$  nm for 515 nm and 1030 nm respectively.

On the biological side, one of the main challenges in this study was the limited number of suitable bioassays. The stents in this study are metallic, have a small diameter and length, an appreciable strut curvature, narrow struts and therefore a small surface area available for cell adherence and growth. Only a small number of cells are available for analysis. Fluorescent microscopy on a non-transparent 3D object is difficult to perform, especially at high magnification. The structure of the stent brings another level of complexity, as cells that are attached on other struts can create a strong fluorescent background, which obstructs focusing on a particular plane

during fluorescent analysis. For any quantitative test like a Live/Dead assay, PicoGreen, Alamar Blue or ELISA, the number of cells per sample that we measured were too low to produce statistically relevant results even when cells demonstrate compatibility with the laser structured surface. Furthermore, in cases when cells failed to adhere it was not possible to detect their presence. Due to these issues, SEM has been chosen as the main technique for characterization of the bio response. It allows us to evaluate sample cytotoxicity and study important parameters such as cell attachment, growth, morphology, activation status for immune cells, cluster formation, fibronectin webbing and protein deposition. None of the tested samples demonstrated significant cytotoxicity as cells with a healthy morphology are present.

It is intriguing that cells showed notable selectivity to the surface modifications on the structured stent. RAW264.7 monocytes have a clear preference for unstructured metal surfaces. Cells were found with healthy morphologies with few that activated into macrophages. Big cell clusters with dense fibronectin connections were also observed. Only swollen dead cells were found on LIPSS surfaces. Factors that can contribute to the adhesion and proliferation of cells on surfaces are surface topography, chemical composition, surface free energy, stiffness and electrostatic charge density. A change in any of these factors could result in the change in response of RAW 264.7. Using a different cell type, Misra et al<sup>43</sup> found that osteoblast cells had the largest response to hydrophilicity and grain structure on the surface of stainless steel.

MS-5 cells failed to make a firm connection with unstructured surfaces. In addition these cells were unable to attach onto the 515 nm LIPSS. In the case of LIPSS generated by 1030 nm, the MS-5 cells attached and formed a monolayer with healthy morphologies. The deeper LIPSS could create a “key-hole” effect thereby allowing the MS-5 cells to attach and proliferate. This demonstrates that MS-5 cells prefer a roughness value of approximately 50 nm. The adhesion, growth and spreading of MS-5 cells on the surface of 1030 nm LIPSS verifies that the surface is non-toxic. HPMEC cells were also examined on the surface of bare and textured stents *in-vitro* yet the results were not consistent. More detailed work is needed to identify surface patterns that suit endothelial cells.

The XPS study was performed to detect chemical changes on the alloy surface after exposure to multiple femtosecond pulses at different laser wavelengths. It was also used to interpret the response from the tested cell lines. From the XPS measurements, it is clear there is a redistribution of elements at the surface after laser exposure. XPS can penetrate the surface to a depth of approximately 10 nm therefore XPS examines the oxide layer and bulk material. Table 2 shows changes to the following elements. The oxide thickness of a bare Pt:SS stent surface is estimated to be 1.5 nm.<sup>44</sup> The oxide thickness of 316LSS was calculated to be 3.6 nm.<sup>45</sup> There is an increase in oxide thickness with an increasing wavelength for Pt:SS. The contrary is observed

for 316LSS, there is a decrease in oxide thickness from 515 nm to 1030 nm. For Pt:SS, there is a 6.3% decrease in Pt at 1030 nm.

It is unlikely that the oxide layer and concentration of Pt is a factor that affects the response of MS-5 and RAW264.7 cells because both alloys have the same cell response. In relation to Cr and Ni, there is a decrease in both elements implying that the surface has become less toxic, except for structures generated on Pt:SS with 515 nm. While this should have a positive impact on the concentration of RAW264.7 cells from bare to 1030 nm the opposite is observed in this study. In the case of bare to 515 nm there is also a decrease in the concentration of Fe. There is an increase in the concentration of Fe from bare to 1030 nm and both alloys have a high percentage of this element present, 37% Fe in Pt:SS and 61-72% in 316LSS. There is no explicit indication on how cells respond to the Fe content in alloys. Some studies show that the cytotoxicity increases in a Fe based alloy *in-vitro*, which reduces viability of fibroblasts<sup>46</sup> while others show an increase in fibroblast proliferation.<sup>47</sup> Based on the XPS results in this study, it is assumed that fibroblasts are susceptible to Cr and Fe, which corresponds to a decrease in Cr and an increase in Fe. It is as yet unclear what chemical changes drive cell response.

### **Conclusion**

Applied threshold fluence values were calculated on Pt:SS and 316LSS at 100 kHz for 30 pulses at 1030 nm and 515 nm. There is a change in the threshold fluence when decreasing wavelength. There is an increase in the LIPSS period and depth with increasing wavelength. Using two wavelengths achieves different topographies. It was found that the parameter to give the highest surface area was 100 kHz at 1030 nm for 30 pulses on Pt:SS with a 32% increase. Also, there is an increase in the roughness with increasing wavelength.

Using SEM, it was determined that different cell types react differently to surface roughness's on a curved surface. Monocytes prefer un-textured surfaces with a roughness value of several nm, while MS-5 cells prefer a surface with a roughness value of approximately 50 nm. Similar cell responses were observed on Pt:SS and 316LSS stent surfaces. On a flat surface it was shown that the number of adhered cells decreases with increasing LIPSS period and depth, confirmed using a live/dead assay. This verifies that cells respond to a change in surface morphology and/or chemistry. This also concludes that with the introduction of LIPSS the surfaces are non-cytotoxic, as healthy morphologies are present. Flat samples were used to prove the biocompatibility of the alloy surface after laser exposure. Because RAW 264.7 and MS-5 cells successfully attached to all un-textured and LIPSS covered surfaces, it is safe to assume that stent topography is a large factor in cell growth. It was found using XPS that the surface chemistry changes from bare to 515 nm and 1030 nm for both Pt:SS and 316LSS. It is assumed that cells respond to changes in Cr and Fe but there is no difference in cell interaction between the two alloys. From this, it is concluded that surface topography generated by ultra-short lasers greatly influences

cell behaviour. The surface chemistry does not change significantly but the topography does. Although this study is performed *in-vitro* one cannot assume the same responses could occur *in-vivo*. A stent could be fabricated with various LIPSS morphologies depending on the application. LIPSS allows one to quickly increase the surface area and roughness of a surface without the use of chemicals. The integration of laser-structured implants with specific topographies may offer new bio-functionalities in the future. The stents used in this study (Pt:SS and 316LSS) have already been developed and approved for clinical relevance. This study focuses on surface modifications on a stent and recording a bio-response. We propose that this *in-vitro* study is a good starting point from which *in-vivo* studies can progress to clinical trials in the future.

### **Acknowledgments**

This work is supported through an IRCSET research grant no. IRCSET-BS-2011-01 and was conducted under the framework of the INSPIRE programme, funded by the Irish Government's Programme for Research in Third Level Institutions, Cycle 4+5, National Development Plan 2007-2013.

This work is supported through an IRCSET research grant no. IRCSET-BS-2011-01 and was conducted under the framework of the INSPIRE programme, funded by the Irish Government's Programme for Research in Third Level Institutions, Cycle 4+5, National Development Plan 2007-2013. Sincere thanks to Pierce Lalor and Dr. Kerry Thompson at the Centre for Microscopy and Imaging (CMI) at the Anatomy Department in NUI, Galway for their assistance.

### **References:**

1. P. T. Mannon, J. Magee, E. Coyne, G. M. O'Connor and T. J. Glynn, *Applied Surface Science*, 2004, 233, 275-287.
2. T. Y. Hwang, A. Y. Vorobyev and C. L. Guo, *Appl. Phys. Lett.*, 2009, 95.
3. T. Y. Hwang and C. L. Guo, *Opt. Lett.*, 2011, 36, 2575-2577.
4. J. Bonse, J. Kruger, S. Hohm and A. Rosenfeld, *J. Laser Appl.*, 2012, 24.
5. I. Martin-Fabiani, E. Rebollar, M. C. Garcia-Gutierrez, D. R. Rueda, M. Castillejo and T. A. Ezquerra, *ACS Appl. Mater. Interfaces*, 2015, 7, 3162-3169.
6. S. Hohm, M. Herzlieb, A. Rosenfeld, J. Kruger and J. Bonse, *Opt. Express*, 2015, 23, 61-71.
7. P. Calvani, A. Bellucci, M. Girolami, S. Orlando, V. Valentini, A. Lettino and D. M. Trucchi, *Appl. Phys. A-Mater. Sci. Process.*, 2014, 117, 25-29.
8. F. Garrelie, J. P. Colombier, F. Pigeon, S. Tonchev, N. Faure, M. Bounhalli, S. Reynaud and O. Parriaux, *Opt. Express*, 2011, 19, 9035-9043.
9. W. Kautek, P. Rudolph, G. Daminelli and J. Kruger, *Appl. Phys. A-Mater. Sci. Process.*, 2005, 81, 65-70.
10. V. S. Mitko, G. R. B. E. Römer, A. J. H. i. t. Veld, J. Z. P. Skolski, J. V. Obona, V. Ocelík and J. T. M. De Hosson, *Physics Procedia*, 2011, 12, Part B, 99-104.
11. C. McDaniel, A. Flanagan and G. M. O'Connor, *Applied Surface Science*, 2014, 295, 1-7.

12. J. Bonse, R. Koter, M. Hartelt, D. Spaltmann, S. Pentzien, S. Hohm, A. Rosenfeld and J. Kruger, *Appl. Phys. A-Mater. Sci. Process.*, 2014, 117, 103-110.
13. J. Eichstadt, G. Romer and A. J. H. In't Veld, *Lasers in Manufacturing 2011: Proceedings of the Sixth International Wlt Conference on Lasers in Manufacturing, Vol 12, Pt B*, 2011, 12, 7-15.
14. P. Roach, D. Farrar and C. C. Perry, *Journal of the American Chemical Society*, 2006, 128, 3939-3945.
15. J. Reif, O. Varlamova, S. Uhlig, S. Varlamov and M. Bestehorn, *Appl. Phys. A-Mater. Sci. Process.*, 2014, 117, 179-184.
16. T. R. Anthony and H. E. Cline, *J. Appl. Phys.*, 1977, 48, 3888-3894.
17. S. Theppakuttai and S. C. Chen, *J. Appl. Phys.*, 2004, 95, 5049-5052.
18. C. Y. Tsai, S. L. Lu, C. W. Hu, C. S. Yeh, G. B. Lee and H. Y. Lei, *Journal of Immunology*, 2012, 188, 68-76.
19. F. Erogbogbo, K. T. Yong, R. Hu, W. C. Law, H. Ding, C. W. Chang, P. N. Prasad and M. T. Swihart, *ACS Nano*, 2010, 4, 5131-5138.
20. Z. D. Xia, L. M. Grover, Y. Z. Huang, L. E. Adamopoulos, U. Gbureck, J. T. Triffitt, R. M. Shelton and J. E. Barralet, *Biomaterials*, 2006, 27, 4557-4565.
21. S. M. Cool, B. Kenny, A. Wu, V. Nurcombe, M. Trau, A. I. Cassady and L. Grondahl, *J. Biomed. Mater. Res. Part A*, 2007, 82A, 599-610.
22. S. H. Lee, M. Senevirathne, C. B. Ahn, S. K. Kim and J. Y. Je, *Bioorg. Med. Chem. Lett.*, 2009, 19, 6655-6658.
23. M. Marchisio, M. Di Carmine, R. Pagone, A. Piattelli and S. Miscia, *J. Biomed. Mater. Res. Part B*, 2005, 75B, 251-256.
24. S. Makihira, Y. Mine, E. Kosaka and H. Nikawa, *Dent. Mater. J.*, 2007, 26, 739-745.
25. M. Oberringer, E. Akman, J. Lee, W. Metzger, C. K. Akkan, E. Kacar, A. Demir, H. Abdul-Khaliq, N. Putz, G. Wennemuth, T. Pohlemann, M. Veith and C. Aktas, *Mater. Sci. Eng. C-Mater. Biol. Appl.*, 2013, 33, 901-908.
26. S. Hamlet and S. Ivanovski, *Acta Biomater.*, 2011, 7, 2345-2353.
27. S. Lee, J. Choi, S. Shin, Y. M. Im, J. Song, S. S. Kang, T. H. Nam, T. J. Webster, S. H. Kim and D. Khang, *Acta Biomater.*, 2011, 7, 2337-2344.
28. B. Zhou, G. Tsaknakis, K. E. Coldwell, C. P. Khoo, M. G. Roubelakis, C. H. Chang, E. Pepperell and S. M. Watt, *Br. J. Haematol.*, 2012, 157, 299-311.
29. H. Hermawan, A. Purnama, D. Dube, J. Couet and D. Mantovani, *Acta Biomater.*, 2010, 6, 1852-1860.
30. G. Rodriguez, M. Fernandez-Gutierrez, J. Parra, A. Lopez-Bravo, M. Molina, L. Duocastella and J. San Roman, *Journal of Bioactive and Compatible Polymers*, 2012, 27, 550-564.
31. K. R. Kranc, H. Schepers, N. P. Rodrigues, S. Bamforth, E. Villadsen, H. Ferry, T. Bouriez-Jones, M. Sigvardsson, S. Bhattacharya, S. E. Jacobsen and T. Enver, *Cell Stem Cell*, 2009, 5, 659-665.
32. R. Berthier, M. H. Prandini, A. Schweitzer, D. Thevenon, H. MartinSisteron and G. Uzan, *Exp. Hematol.*, 1997, 25, 481-490.
33. H. Kenar, E. Akman, E. Kacar, A. Demir, H. Park, H. Abdul-Khaliq, C. Aktas and E. Karaoz, *Colloid Surf. B-Biointerfaces*, 2013, 108, 305-312.
34. B. R. Prasad, M. A. Brook, T. Smith, S. G. I. Zhao, Y. Chen, H. Sheardown, R. D'Souza and Y. Rochev, *Colloid Surf. B-Biointerfaces*, 2010, 78, 237-242.

35. C. P. Pennisi, C. Sevcencu, A. Dolatshahi-Pirouz, M. Foss, J. L. Hansen, A. N. Larsen, V. Zachar, F. Besenbacher and K. Yoshida, *Nanotechnology*, 2009, 20.
36. L. Li, N. Mirhosseini, A. Michael, Z. Liu and T. Wang, *Lasers Surg. Med.*, 2013, 45, 608-616.
37. J. M. Liu, *Opt. Lett.*, 1982, 7, 196-198.
38. D. Bauerle, *Laser Processing and Chemistry*, Springer, 4 edn., 2011.
39. M. B. a. C. B. Arnold, *Fundamentals of Laser-Material Interaction and Application to Multiscale Surface Modification*, Springer, 2010.
40. J. Houard, A. Vella, F. Vurpillot and B. Deconihout, *Phys. Rev. B*, 2011, 84.
41. *Fundamentals of Laser-Assisted Micro- and Nanotechnologies*, Springer, 2014.
42. M. Tsukamoto, D. Tone, T. Shibayanagi, S. Motokoshi, M. Fujita and N. Abe, *Transactions of JWRI*, 2010, 39, 1-4.
43. R. D. K. Misra, C. Nune, T. C. Pesacreta, M. C. Somani and L. P. Karjalainen, *Acta Biomater.*, 2013, 9, 6245-6258.
44. B. J. O'Brien, J. S. Stinson, S. R. Larsen, M. J. Eppihimer and W. M. Carroll, *Biomaterials*, 2010, 31, 3755-3761.
45. T. Hanawa, S. Hiromoto, A. Yamamoto, D. Kuroda and K. Asami, *Mater. Trans.*, 2002, 43, 3088-3092.
46. B. Liu and Y. F. Zheng, *Acta Biomater.*, 2011, 7, 1407-1420.
47. F. L. Nie, Y. F. Zheng, S. C. Wei, C. Hu and G. Yang, *Biomed. Mater.*, 2010, 5.